BIOPHYSICS AND BASIC BIOMEDICAL RESEARCH – Full Papers

Magnetic Resonance in Medicine 80:317–329 (2018)

Relationships Between Tissue Microstructure and the Diffusion Tensor in Simulated Skeletal Muscle

David B. Berry,[1] Benjamin Regner,[2] Vitaly Galinsky,[2] Samuel R. Ward,[1,3,4] and Lawrence R. Frank[3]*

Purpose: To establish a series of relationships defining how muscle microstructure and diffusion tensor imaging (DTI) are related.
Methods: The relationship among key microstructural features of skeletal muscle (fiber size, fibrosis, edema, and permeability) and the diffusion tensor were systematically simulated over physiologically relevant dimensions individually, and in combination, using a numerical simulation application. Stepwise multiple regression was used to identify which microstructural features of muscle significantly predict the diffusion tensor using single-echo and multi-echo DTI pulse sequences. Simulations were also performed in models with histology-informed geometry to investigate the relationship between fiber size and the diffusion tensor in models with real muscle geometry.
Results: Fiber size is the strongest predictor of $\lambda 2$, $\lambda 3$, mean diffusivity, and fractional anisotropy in skeletal muscle, accounting for approximately 40% of the variance in the diffusion model when calculated with single-echo DTI. This increased to approximately 70% when diffusion measures were calculated from the short T_2 component of the multi-echo DTI sequence. This nonlinear relationship begins to plateau in fibers with greater than 60-μm diameter.
Conclusions: As the normal fiber size of a human muscle fiber is 40 to 60 μm, this suggests that DTI is a sensitive tool to monitor muscle atrophy, but may be limited in measurements of muscle with larger fibers. **Magn Reson Med 80:317–329, 2018. © 2017 International Society for Magnetic Resonance in Medicine.**

Key words: DTI; skeletal muscle; multi-echo DTI; muscle microstructure; diffusion; simulation

INTRODUCTION

Skeletal muscle is a highly organized, hierarchical tissue containing long contractile cells bundled to form fascicles, which are again bundled to form the larger whole muscle (1). These subdivisions of muscle are all packaged in layers of extracellular matrix (ECM). With injury, microstructural (cell-level) changes have been observed, which are related to impaired muscle function (2,3). Commonly observed changes in muscle microstructure with injury or pathology include fiber atrophy/hypertrophy (4,5), fibrosis (6), membrane damage (permeable fibers) (7–9), and edema (10–12). The current gold standard for studying injury- or plasticity-associated changes in muscle microstructure is histology, which is highly invasive, is semi-quantitative, and difficult to extrapolate to the entire muscle. Therefore, a quantitative, noninvasive technique to study muscle microstructural changes resulting from injury would be a potentially important contribution to the clinical assessment of muscle pathologies.

Diffusion tensor imaging (DTI) is an MRI technique that has been shown to be sensitive to changes in muscle microstructure (13–15). Diffusion tensor imaging measures the anisotropic diffusion of water in muscle, which is restricted by microstructure. However, the relationship among microstructure, the actual diffusion changes, and the resultant diffusion tensor (DT) associated with muscle injury or pathology are exceedingly complex and not amenable to simple analysis. Nevertheless, certain structural and physiological quantities averaged over the voxel volume can serve as a proxy for actual structural features and their changes. For example, several groups have shown a less-restricted diffusion profile when muscles are shortened, and a more restricted diffusion profile when muscles are elongated (16–20). This effect is attributed to changes in muscle-fiber diameter that occur when a whole muscle is contracted (fiber diameter increases) or elongated (fiber diameter decreases). However, such a simple explanation is complicated in injured states, as less restricted diffusion is also observed when edema is present or structural integrity of the sarcolemma is compromised (fibers are more permeable to water exchange between the intra- and extracellular compartments), regardless of underlying changes in muscle fiber diameter (4,21,22). In addition to changes in the permeability of the sarcolemma and size of fibers, diffusion changes have been attributed to increases in T_2, which results in increased signal-to-noise ratio, secondary to increased extracellular fluid volume (23–25).

[1]Department of Bioengineering, University of California San Diego, La Jolla, California, USA.
[2]Institute of Engineering in Medicine, San Diego, California, USA.
[3]Department of Radiology, University of California San Diego, La Jolla, California, USA.
[4]Department of Orthopedic Surgery, University of California San Diego, La Jolla, California, USA.
*Correspondence to: Lawrence R. Frank, Ph.D., Department of Radiology, University of California San Diego, 9500 Gilman Drive (0854), La Jolla, CA 92093, USA. E-mail: lfrank@ucsd.edu

L.R.F. is supported by grants from the National Institutes of Health (R01AR070830, R01MH096100, and R01AG054049) and National Science Foundation (DBI-1147260, ACI-1550405, ACI-1440412, and AA013419-12). S.R.W. is supported by grants from the National Institutes of Health (R01AR070830, R01HD073180, and R01HD088437) and Department of Defense (PR120576).
Received 13 April 2017; revised 11 October 2017; accepted 12 October 2017
DOI 10.1002/mrm.26993
Published online 31 October 2017 in Wiley Online Library (wileyonlinelibrary.com).

Nondiffusion, MR relaxometry experiments can uncover these edema-related fluid shifts involved in maintaining metabolic and volumetric stasis among the intracellular compartments (4,12,26,27), but lacks the ability to resolve microstructural features of muscle, which directly inform physiology and performance.

Muscle exhibits a multi-exponential T_2 decay signal of water, which originates from macromolecular interactions (ultrashort; < 5 ms), intracellular (short T_2; 20–40 ms), and extracellular (long T_2; $90+$ ms) compartments of muscle (26–30). The ultrashort T_2 compartment is often too short to be measured using spin-echo imaging as a result of requisite echo times, and is mostly ignored (10). In the presence of edema, increased fluid content is observed in the extracellular space around cells (11,31). Because of the changes in cellularity observed during edema, as the volume fraction of extracellular water increases, whole-muscle T_2 increases. However, whole-muscle T_2 can also be traced to intracellular origins (24,26,32). Although simplification of T_2 decay into a one-compartment model is adequate for normal muscle, injured or pathologic muscle exhibits multiple microstructural changes, including edema, which renders a single-compartment model too simple (10,12,30). One approach to addressing this complication is multi-echo DTI, an MR technique that combines basic principles to simultaneously measure T_2 and the DT, which allows quantification of diffusion originating from the short (intracellular) and long (extracellular) compartments of muscle (10,12). This technique has the potential to increase the specificity of DTI to be a better tool to measure changes in muscle microstructure.

The complexity of the relationship between muscle microstructure and the diffusion profile in both normal and injured muscle thus requires a systematic investigation if useful clinical metrics are to be derived from the measured diffusion signal. The effect of muscle microstructural changes on the measured DT can be quantified by computer simulation. Several groups have investigated the effect of imaging parameters such as noise, partial volume, and diffusion weighting strength on the DT, to inform guidelines for developing DTI protocols (23,25,33–35). Other studies have simulated the effect of fiber geometry, edema, atrophy, and permeability, on the diffusion signal in muscle (21,36,37). In this paper, we use the DTI simulation application DifSim, which is capable of modeling an entire DTI experiment with complex tissue geometries.

Therefore, the purpose of this study is to use a novel, sophisticated, in silico tool to carefully investigate the relationships between both simplified and histology-informed muscle microstructure and the DT. Specifically, we will quantify the influence of muscle fiber size, fibrosis, injury-induced membrane permeability, and edema, in isolation and in combination, on the DT using single- and multi-echo DTI techniques. We hypothesize that intra- and extracellular microstructural changes in injured muscle have characteristic diffusion profiles that can be uncoupled with multi-echo DTI.

METHODS

Overview of DifSim

DifSim embeds MCell, a Monte Carlo simulator for cellular microphysiology (38–40), within an MRI simulator that tracks particle location, magnetization amplitude, and phase within a user-defined arbitrarily complex geometrical model (41). DifSim is capable of supporting boundary and particle interactions, and multiple molecular species with different diffusion coefficients.

The basic numerical approach of DifSim is presented here. A more complete treatment of DifSim can be found in (41). A more complete treatment of MCell can be found in (38–40). Particles (spins) diffusing in time (t) at a position ($x(t)$) have a spin (j) and will accrue a phase (θ_j) generated by the spin's displacement in the direction of the magnetic field (G(t)) gradient as follows:

$$\theta_j(t) = \int_{t_0}^{t} G(\tau) \cdot x_j(\tau) d\tau \quad [1]$$

If time is discretized into N_t time steps of length dt, and measures the magnetic field strength and spin location at each time t_i, Equation [1] can be approximated as

$$\theta_j(t) = \sum_{i=0}^{N_t} G(t_i) \cdot x_j(t_i) dt \quad [2]$$

The relaxation is introduced for each particle j at each time t_i by using particle magnetization vector

$$(m_x^j, m_y^j, m_z^j) = \left(m_\rho^j cos(\theta_j), m_\rho^j sin(\theta_j), m_z^j\right) \quad [3]$$

as

$$m_\rho^j = m_\rho^j(0) e^{-t/T_2} \quad [4]$$

$$m_z^j = m_z^j(0) e^{-t/T_1} + (1 - e^{-t/T_1}) \quad [5]$$

By simultaneously simulating the diffusion of N_p individual spins with MCell, the echo amplitude becomes

$$E = \frac{e^{-t/T_2}}{N_p} \sum_{j=1}^{N_p} e^{i\gamma\theta_j} \quad [6]$$

where γ is the gyromagnetic ratio.

Simulation DTI Pulse-Sequence Parameters

The pulse-sequence parameters used in our MRI simulations were based on those used on a 7T MRI scanner at our institution (Bruker, Billerica, MA, USA) (42). A diffusion-weighted, multi-echo pulse sequence was used (12). The first echo was echo time (TE) = 21.76 ms, with 16 equally spaced echoes at 10-ms intervals, 15 gradient directions, $b = 500\,mm^2/s$ (δ/Δ 2 ms/9 ms), and voxel size $200 \times 200 \times 200\,\mu m^3$.

Simulation Details

Simulations were performed on one of four Linux clusters (Supporting Table S1). The total number of computer hours for all simulations was 27 years, 51 weeks.

The smallest barrier spacing encountered by particles was $1\,\mu m$. In MCell, diffusion steps are not set to a fixed length, but are chosen to match the probability

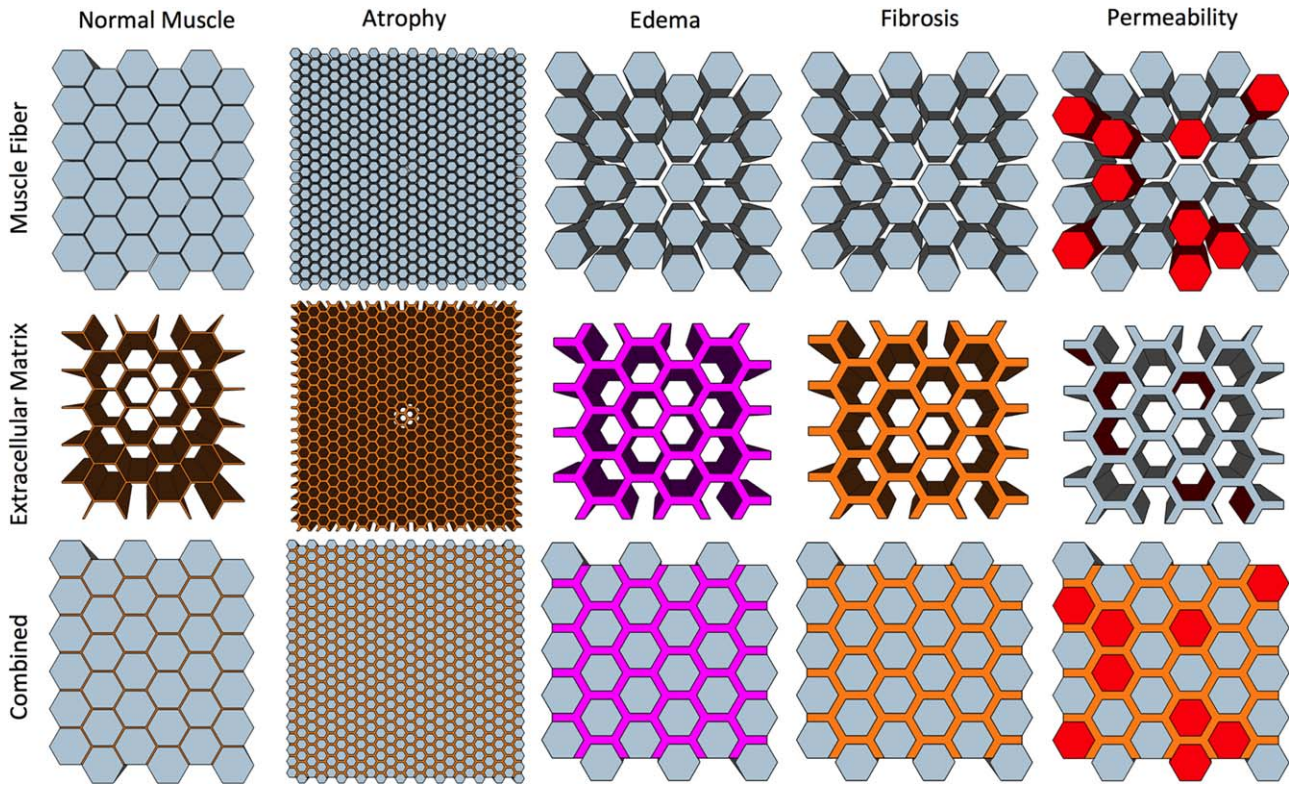

FIG. 1. Schematic depicting ideally shaped hexagonal models of skeletal muscle (top row; intracellular) and the ECM (middle row; extracellular). Atrophy/hypertrophy was simulated by changing the diameter of the muscle fibers; edema was simulated by changing the extracellular water-volume fraction; fibrosis was simulated by changing the spacing between muscle fibers; and permeability was simulated by allowing free transport between fiber walls into the ECM (red).

distribution of the unbounded diffusion over the length of a single time step. The average distance that a molecule could move during a step was 96 nm.

Diffusion Tensor Calculation

For each voxel, the DT was calculated using single-echo data (Eq. [7a]) and as two compartments in slow exchange (Eq. [7b]) from multi-echo data using custom-written software in MATLAB (MathWorks, Natick, MA, USA):

$$S_i(b)/S_0 = e^{(-bD_i)} + \varepsilon \quad [7a]$$

$$S_i(TE,b)/S_0 = f_a e^{\left(\frac{-TE}{T_{2,a}}\right)} e^{(-bD_{i,a})} + f_b e^{\left(\frac{-TE}{T_{2,b}}\right)} e^{(-bD_{i,b})} + \varepsilon \quad [7b]$$

where $S_i(TE,b)$ is the signal along a certain gradient direction (S_i) at TE and b-value (b), f is the volume fraction of the short (f_a) and long (f_b) T_2 compartments of the apparent diffusion coefficient (D_i) along the same gradient direction, such that $f_a + f_b = 1$.

First, a bi-exponential decay function was fit from the b = 0 image from each echo using the MERA 2.03 toolbox to find $f_a, f_b, T_{2,a}$, and $T_{2,b}$ (43). A nonlinear least squares fit was used to solve $D_{i,a}$ and $D_{i,b}$ using the *fit* function in MATLAB (lower limit = 0 mm^2/s; upper limit = 1 mm^2/s). The DT was solved using a nonnegative least-squares fit using the fanDTasia toolbox (44). Diagonalization of the DT yields the eigenvalues (λ1, λ2, and λ3), which were used to calculate the mean diffusivity (MD) and fractional anisotropy (FA) (Eqs. [8] and [9]). For single-echo analysis, data from the first recorded echo of the multi-echo DTI sequence were used.

$$MD = \frac{\lambda 1 + \lambda 2 + \lambda 3}{3} \quad [8]$$

$$FA = \sqrt{\frac{3}{2}} \sqrt{\frac{(\lambda 1 - MD)^2 + (\lambda 2 - MD)^2 + (\lambda 3 - MD)^2}{\sqrt{\lambda 1^2 + \lambda 2^2 + \lambda 3^2}}} \quad [9]$$

Fractional anisotropy is a normalized scalar measure of how anisotropic the diffusion profile is, and varies from 0 (perfectly isotropic) to 1 (perfectly anisotropic). Mean diffusivity is a measure of the average overall diffusion. Mean diffusivity of unrestricted water is 2.5 × 10^{-3} mm^2/s. Generally, as the restricted diffusion profile increases (increased FA), there is less overall diffusion (decreased MD) and vice versa.

Simplified Model Generation

As a first step, the complex geometry of skeletal muscle was reduced to simple, closely packed hexagons, which have a limited number of defining parameters that allowed us to systematically study the relationship between an idealized muscle microstructure model and the measured DT. The features of the studied muscle microstructure include fiber size, fibrosis, edema, and permeability, and are depicted in Figure 1. Ideal muscle model geometries were simplified into geometrically symmetric patterns in the x-y axis, and extruded linearly

Table 1
Microstructural Features and the Range Over Which They Were Varied Individually and in Combination of Muscle With Simplified Geometry

				Step	
Microstructure	Units	Lower bound	Upper bound	Individual	Interactions
Fiber size	μm	10	100	10	20
Permeability	% transparent fibers	0	60	20	20
Fibrosis	μm	1	10	1	2
Edema	Extracellular volume fraction	5	50	5	10

along the z-axis, which approximates but not exactly replicates real muscle microstructure. Fiber size was varied by systematically changing the diameter of the hexagon structures. Fibrosis was modeled by varying the spacing between muscle fibers. Edema was simulated by varying the volume fraction of water in the extracellular space. Permeability changes caused by structural defects in a muscle fiber were varied by randomly defining walls of the fibers as transparent to water molecules, to diffuse between the intra- and extracellular spaces.

Microstructural features of skeletal muscle were varied individually and in combination over a range of physiologically relevant values (Table 1) to determine their individual contributions to the DT, individually, and in combination with one another. The basic model that represents normal healthy muscle was defined with 50-μm fiber diameter, 2-μm fiber spacing, 5% extracellular water-volume fraction, and 0% permeable walls. Individual features of muscle microstructure were investigated based on this model. Models were constructed in Google SketchUp, and triangulated using Blender (45). Intra- and extracellular particles were assigned different diffusion coefficients and magnetic relaxation (T_1, T_2) rates based on literature values. Relaxation rates and diffusion coefficients of molecular species were taken from the literature: intracellular (T_1/T_2: 1,740/25 ms (12,46,47), D: $1.8*10^{-3}$ mm^2/s (48–50)); and extracellular (T_1/T_2: 2500/95 ms (12,47), D: $2.2*10^{-3}$ mm^2/s (51,52)). A total of 200,000 particles were simulated to accurately converge on an analytical solution based on the diffusion coefficients and b-value chosen for this experiment (41). Each model was simulated 10 times with a different initial location of diffusing particles to measure variance in an individual model. No noise was added to measure the exact relationship between muscle microstructure and the DT under ideal imaging conditions. Myofilaments within a muscle fiber, or extracellular matrix proteins outside of muscle fibers, were not physically defined in this model. However, restricted diffusion from myofilaments and extracellular matrix proteins is at least partially reflected in the assignment of diffusion coefficients from previous studies of diffusion of small molecules in these tissues.

Histology-Informed Geometry Models

To evaluate how our results compare with real diffusion measurements of muscle, we created models with geometry derived from previous animal histology experiments. Masson's trichrome stained histology of muscle fibers from control, cardiotoxin-injected, botulinium toxin (botox) injected, surgically denervated, and surgically tenotomized rat tibialis anterior muscles at 1, 3, 7, 14, and 30 days after injury were manually segmented and triangulated in a blender (Fig. 2). Cardiotoxin is venom from the Naja mossambica snake, and induces depolarization of the sarcolemma that results in a massive, rapid onset muscle degeneration from which muscle can heal in approximately 30 days (53). Botox is a bacterium-produced neurotoxin that prevents acetylcholine release in motor neurons and results in muscle atrophy (3). Surgical denervation creates a physical nerve injury that prevents a muscle from contracting, resulting in chronic atrophy (54). Surgical tenotomy severs the tendon that attaches muscle to bone, resulting in acute fiber hypertrophy caused by isometric contraction of the muscle, followed by chronic atrophy (55). Average fiber diameters were recorded for each model. Each histological image was separated into nine individual diffusion experiments, covering a total volume of $600 \times 600 \times 200\,\mu m^3$. Extracellular water-volume fractions assigned to each model are defined in Table 2 and are approximated from histologic and MRI studies of these tissues. The same relaxation and diffusion coefficients assigned to the simplified models of muscle were applied to the histology-informed models.

Statistics

The relationship between individual features of muscle microstructure and the DT were quantitatively examined. To determine how the interaction between different compartments of muscle microstructure and the DT (FA and MD) are related, a stepwise multiple linear regression model was used.

To demonstrate the difference in the DT measured with single- and multi-echo DTI, a curve was fit to describe the relationship fiber size and the DT for simplified, non-edematous models using the single-echo data. Then, the same fiber size models were simulated with edema (45% extracellular water-volume fraction) and the DT calculated with both single- and multi-echo DTI data. The relationship among the single, short, and long DTs and fiber size in edematous muscle were compared with the nonedematous curve. A coefficient of determination (R^2) was calculated to measure the amount of variance explained by the original model and the edematous DTs. Then, the same equations were compared with the single, short, and long DTs in models with histology-informed geometry.

The threshold for significance (α) was set to 0.05 for all analyses. Statistics were computed using SPSS 20.0 (IBM, Armonk, NY). All data are reported as mean ± standard deviation.

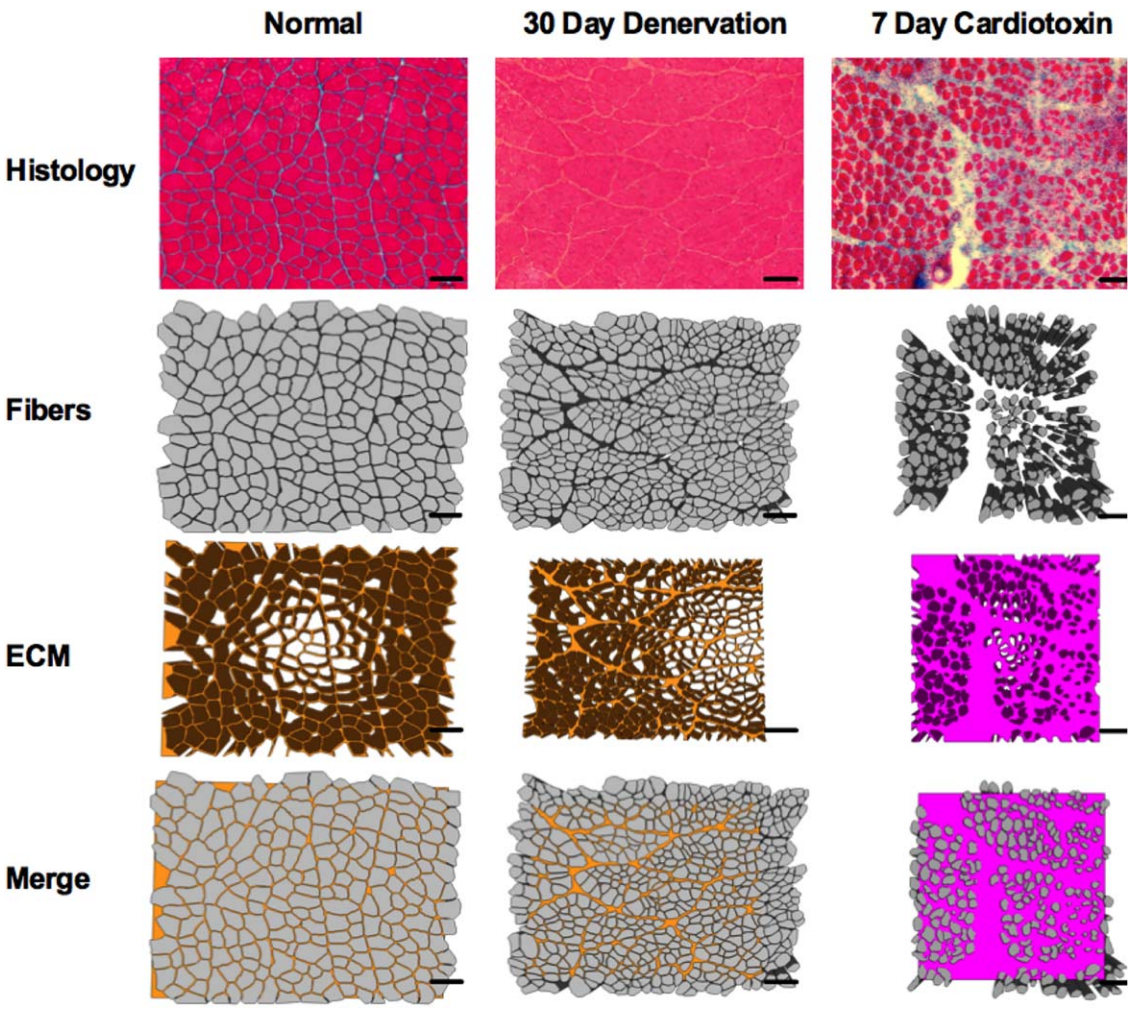

FIG. 2. Schematic depicting sample histology-informed models of skeletal muscle. Fibers were manually traced from histology images.

RESULTS

Individual Relationships Between Simplified Muscle Geometry and the Measured DT

Of the independent features studied, fiber size has the largest dynamic range of the microstructural features examined in this study. Above a 60-μm diameter, the relationship between fiber size and the DT appears to reach a plateau (Figs. 3a and 3d; Supporting Figs. S1a, S1e, and S1i). The single-echo and short compartment of the multi-echo DTI pulse sequences appear to be nearly identical, as fiber size, fibrosis, and permeability was varied (Figs. 3a, 3b, 3d–3f, and 3h; Supporting Figs. S1a and S1b, S1d–S1F, S1h–S1j, and Sl). However, as extracellular water volume is increased (muscle becomes more edematous), the single-echo DTI measurements appear to become more similar to the long compartment of the multi-echo DTI measurements (Figs. 3c and 3g; Supporting Figs. S1c and S1g). Interestingly, there is no change in either the short- or long-compartment diffusion measurements as the extracellular water-volume fraction is increased. The relationships between microstructure and the DT were nearly identical between λ2 and λ3 (Supporting Figs. S1e–S1l).

Table 2
Extracellular Water-Volume Fractions Applied to Models With Histology-Informed Geometry

	Day 1	Day 3	Day 7	Day 14	Day 30
Control	5	5	5	5	5
Botox	20	15	10	10	10
Denervation	10	10	10	10	10
Tenotomy	10	5	5	5	5
Cardiotoxin	X	45	35	10	5

Predictive Capacity of Muscle Microstructure on the DT

Ten replicates of 500 models were input into the stepwise multiple linear regression model to determine which features of microstructure are the best predictors of the DT. As fiber size has a strong nonlinear relationship to the DT, it was $\log_e$-transformed for all statistical analysis. Using single-echo DTI, fiber size was the best predictor of MD, λ2, λ3, and FA, explaining 40.7 to 44.9% of the variance respectively (Table 3). The next-best microstructural predictor of MD, λ2, λ3, and FA was permeability, explaining 29 to 35.7% of the variance. Edema and fibrosis together explain 3.1 to 6.4% of variance for MD, λ2, λ3, and FA. Fiber size, permeability,

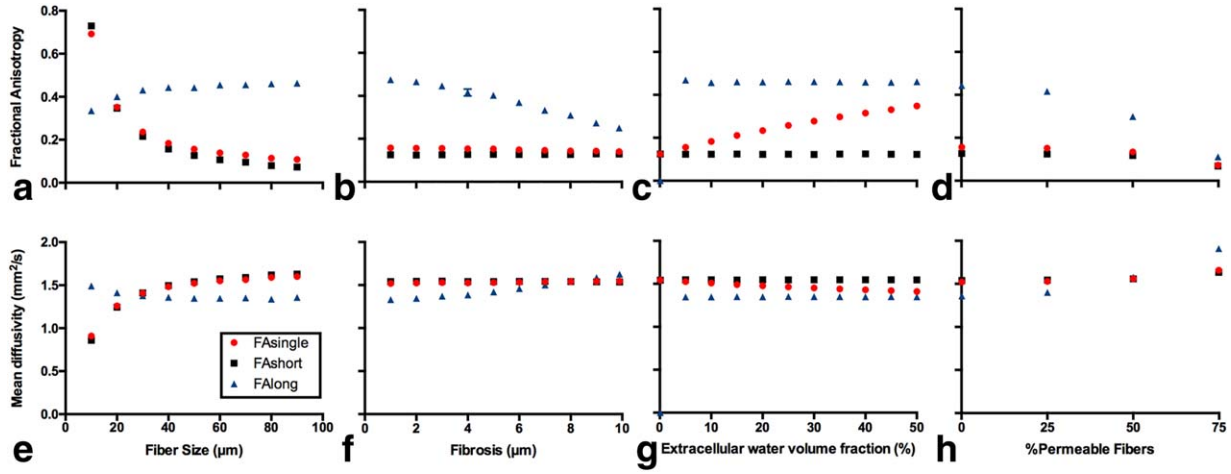

FIG. 3. Fractional anisotropy (**a–d**) and mean diffusivity measurements (**e–h**) measurements of simplified models of skeletal muscle. Diffusion measurements were made from single-echo DTI (red circles) and the short (black squares) and long (blue triangles) T_2 compartments from the multi-echo DTI sequence. Fiber size (**a, e**), fibrosis (**b, f**), edema (**c, g**), and permeability (**d, h**) were varied over a physiologically relevant range of parameters defined in Table 1.

and fibrosis are positively correlated with MD, λ2 and λ3, and negatively correlated with FA. Edema is positively correlated with MD and FA. Interestingly, edema was a strong predictor of λ1 ($R^2 = 0.98$, $\beta = 0.990$), with fibrosis ($R^2 = 0.003$ $\beta = -0.046$) and fiber size ($R^2 < 0.001$, $\beta = 0.018$) also significant predictors in the model.

Diffusion in the short T_2 compartment calculated with multi-echo DTI was hypothesized to represent intracellular diffusion. Similar to single echo, fiber size is a strong predictor of the short compartment of MD, λ2, λ3, and FA, explaining 70.7 to 76.2% of the variance in the model (Table 3). Additionally, permeability ($R^2 = 0.098$–0.106) and fibrosis ($R^2 = 0.001$–0.002) were significant predictors of MD, λ2, λ3, and FA. Fiber size, permeability, and fibrosis are positively correlated with MD, λ2 and λ3, and negatively correlated with FA. Permeability ($\beta = -0.132$), fiber size ($\beta = -0.090$), and edema ($\beta = 0.054$) were all found to be significant predictors of λ1; however, these microstructural measurements explain only 2.9% of the variance in the model.

Diffusion in the long T_2 compartment calculated with multi-echo DTI was hypothesized to represent extracellular diffusion. Permeability was the best predictor of MD, λ2, and FA ($R^2 = 0.615$–0.669), followed by fibrosis ($R^2 = 0.135$–0.177) then fiber size ($R^2 = 0.044$–0.075; Table 3). Permeability and fibrosis are positively correlated with MD and λ2, and negatively correlated with FA. Fiber size is negatively correlated with MD and λ2, and positively correlated with FA. Unexpectedly, fiber size was the strongest predictor of λ3 ($R^2 = 0.756$, $\beta = 0.870$), followed by permeability ($R^2 = 0.106$, $\beta = 0.325$) and fibrosis ($R^2 = 0.001$, $\beta = 0.037$). All four microstructural features tested were significant predictors of λ1; however, the total variance explained by the model was relatively low ($R^2 = 0.249$) compared with the other dependent variables.

Resolution of Fiber-Size Measurements Using Multi-echo DTI

The relationship between fiber size and FA calculated from single-echo DTI for normal (5% extracellular water-volume fraction) simplified muscle was fit to an exponential decay equation, which explained 99.5% of the variance in the data (Fig. 4a). When fiber size and FA were simulated under edematous conditions (45% extracellular water-volume fraction), the original equation explained none of the variance when FA was calculated from single-echo DTI data ($R^2 = -5.68$) or from the long T_2 compartment using multi-echo DTI analysis ($R^2 = -76.8$), and 97.9% of the variance of FA calculated from the short T_2 compartment using multi-echo DTI data. Similarly, the relationship between fiber size and MD calculated from single-echo DTI for normal simplified muscle was fit to a one-phase association equation, which explained 99.6% of the variance in the data (Fig. 4b). When fiber size and MD were simulated under edematous conditions, the original equation explained none of the variance when MD was calculated from single-echo DTI data ($R^2 = -1.55$) or from the long T_2 compartment using multi-echo DTI analysis ($R^2 = -35.1$), and 98.7% of the variance of FA calculated from the short T_2 compartment using multi-echo DTI data.

Histology-Informed Muscle Geometry

Models were simulated at all time points except for the cardiotoxin Day 1 injury, as these muscle fibers had no discernable organized structure. The mean fiber size ranged from 35 to 76 μm in diameter (Fig. 5). In general, botox and denervation models had the smallest fibers, which decreased in size over time. The average fiber size of the cardiotoxin model steadily increased over the 30-day time course.

Diffusion measurements in control muscle show little change over the course of 30 days with single-echo DTI (Figs. 6a and 6d). Large differences in FA were observed between Day 3 ($FA = 0.12 \pm 0.01$), Day 7 ($FA = 0.22 \pm 0.05$), and Day 14 ($FA = 0.14 \pm 0.03$) in the cardiotoxin model when calculated using single-echo DTI, which were not reflective of the measured fiber-size changes (Figs. 5 and 7a). However, when FA was calculated from

Table 3
Stepwise Linear Regression Results

DTI analysis	Diffusion measure	Microstructure	β	Standardized β	R^2
Single echo	λ1	Constant	1.78^{-3}		
		Edema	4.64^{-6}	0.990	0.980
		Fibrosis	-1.08^{-6}	−0.046	0.983
		Fiber size	1.55^{-6}	0.018	0.983
	λ2	Constant	1.59^{-4}		
		Fiber size	2.39^{-4}	0.670	0.449
		Permeability	5.77^{-4}	0.581	0.787
		Fibrosis	1.65^{-5}	0.168	0.815
		Edema	1.79^{-6}	0.091	0.823
	λ3	Constant	2.02^{-4}		
		Fiber size	2.22^{-4}	0.638	0.407
		Permeability	5.78^{-4}	0.597	0.763
		Fibrosis	1.68^{-5}	0.176	0.794
		Edema	1.23^{-6}	0.064	0.798
	MD	Constant	7.14^{-4}		
		Fiber size	1.54^{-4}	0.646	0.417
		Permeability	3.85^{-4}	0.580	0.754
		Edema	2.55^{-6}	0.195	0.791
		Fibrosis	1.07^{-5}	0.164	0.818
	FA	Constant	7.49^{-1}		
		Fiber size	-1.14^{-1}	−0.661	0.437
		Permeability	-2.59^{-1}	−0.539	0.727
		Fibrosis	-7.95^{-3}	−0.168	0.755
		Edema	5.89^{-4}	0.062	0.759
Multi-echo (short T_2)	λ1	Constant	1.77^{-3}		
		Permeability	-3.16^{-6}	−0.132	0.018
		Fiber size	-7.72^{-7}	−0.090	0.026
		Edema	2.52^{-8}	0.054	0.029
	λ2	Constant	-2.91^{-4}		
		Fiber size	3.99^{-4}	0.873	0.762
		Permeability	4.11^{-4}	0.324	0.866
		Fibrosis	4.20^{-6}	0.033	0.867
	λ3	Constant	-2.82^{-4}		
		Fiber size	3.91^{-4}	0.870	0.756
		Permeability	4.07^{-4}	0.325	0.862
		Fibrosis	4.54^{-6}	0.037	0.864
	MD	Constant	3.99^{-4}		
		Fiber size	2.63^{-4}	0.871	0.758
		Permeability	2.72^{-4}	0.323	0.863
		Fibrosis	2.89^{-6}	0.035	0.864
	FA	Constant	1.05		
		Fiber size	-2.10^{-1}	−0.841	0.707
		Permeability	-2.17^{-1}	−0.313	0.806
		Fibrosis	-2.15^{-3}	−0.031	0.807
Multi-echo (long T_2)	λ1	Constant	2.11^{-3}		
		Permeability	2.89^{-5}	0.362	0.131
		Fibrosis	-2.26^{-6}	−0.286	0.213
		Fiber size	4.36^{-6}	0.152	0.236
		Edema	1.82^{-7}	0.115	0.249
	λ2	Constant	1.24^{-3}		
		Permeability	8.35^{-4}	0.821	0.673
		Fibrosis	3.86^{-5}	0.384	0.821
		Fiber size	-7.63^{-5}	−0.209	0.865
	λ3	Constant	-2.82^{-4}		
		Fiber size	3.91^{-4}	0.870	0.756
		Permeability	4.07^{-4}	0.325	0.862
		Fibrosis	4.54^{-6}	0.037	0.864
	MD	Constant	1.55^{-3}		
		Permeability	5.66^{-4}	0.818	0.669
		Fibrosis	2.52^{-5}	0.368	0.805
		Fiber size	-6.03^{-5}	−0.243	0.863
	FA	Constant	3.07^{-1}		
		Permeability	-3.27^{-1}	−0.784	0.615
		Fibrosis	-1.74^{-2}	−0.421	0.792
		Fiber size	4.12^{-2}	0.275	0.867

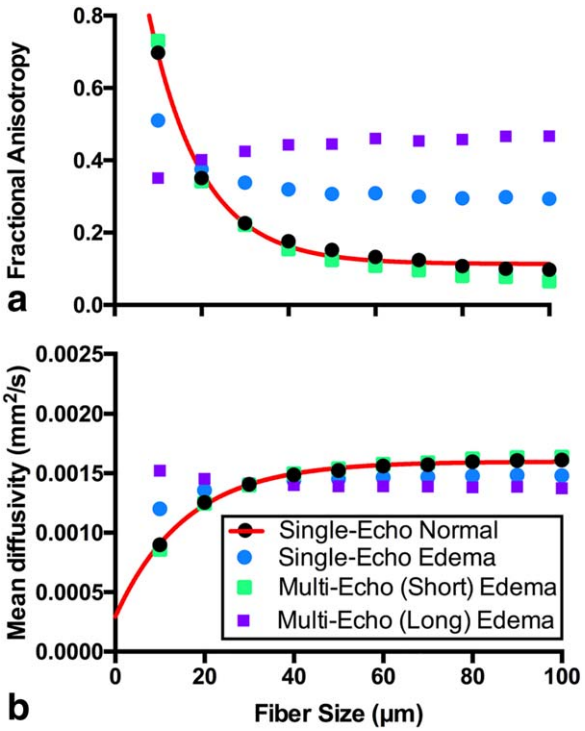

FIG. 4. Fractional anisotropy (**a**) and mean diffusivity (**b**) measurements as a function of fiber diameter measured with single-echo (circles) and multi-echo (squares) DTI for normal (black; 5% extracellular water-volume fraction) and edematous (45% extracellular water-volume fraction) muscle. Nonlinear regression (red line) was fit to the normal muscle diffusion measurements measured with single-echo DTI. The equation for the fractional anisotropy regression is $FA = (1.432 - 0.1134) * e^{-0.082 * \text{fibersize}} + 0.1134$. The equation for the mean diffusivity regression is $MD = 2.94 * 10^{-4} \ \frac{mm^2}{s} + \left(1.30 * 10^{-3} \frac{mm^2}{s}\right) * (1 - e^{-.064 * \text{fibersize}})$.

the short compartment of the multi-echo DTI analysis, FA appeared to steadily decrease over this time period, which better reflects fiber-size changes at these time points (Figs. 6b and 7b). Botox and denervation models had the highest FA measurements when measured with both single- and multi-echo DTI, especially at later times points when fibers were smaller. In general, MD measurements made with single and the short compartment of multi-echo DTI displayed similar trends, although the short compartment measured MD had higher overall diffusivity measurements, likely because of a higher defined diffusion coefficient. The FA and MD measurements calculated from the long compartment of multi-echo DTI demonstrated very high FA and low MD, likely because of the highly restricted diffusion environment of the extracellular space between fibers (Figs. 6c and 6f). Unlike the ideal models of muscle microstructure, no similarity was observed between $\lambda 2$ and $\lambda 3$ in models with histology-informed geometry (Supporting Fig. S2).

To compare how well diffusion measurements made in the simplified hexagonal models of muscle are to diffusion measurements made in models with histology-informed geometries, we compared the equations fit between fiber size and diffusion measurements (FA and MD) for normal (5% extracellular water-volume content) muscle with ideal geometry to histology-informed measures of diffusion (Fig. 7). The equation relating fiber size to FA in models with ideal muscle geometry explained none of the variance in FA when calculated with single echo ($R^2 = -0.156$) or the long compartment of multi-echo DTI ($R^2 = -10.9$). However, this equation described 68.6% of the variance in FA when calculated with the short compartment of multi-echo DTI. The equation relating fiber size to MD in models with ideal muscle geometry described none of the variance in MD when calculated with single echo ($R^2 = -3.21$), the short compartment ($R^2 = -9.12$), or the long compartment ($R^2 = -6.50$) using multi-echo DTI. (A negative R^2 is possible when a model is forced to fit data and the fit is worse than a horizontal line or the mean of the dependent variable.)

DISCUSSION AND CONCLUSIONS

The use of DTI to characterize muscle structure and physiology is an active area of research with important clinical implications informing guidelines for developing DTI protocols specific to skeletal muscle (23,25,33–35). However, the complexity of the relationship between muscle health and the measured DT continues to limit DTI's clinical utility.

The multi-echo DTI is not novel to this study and has been performed previously and reported in the literature. Van Dusschoten pioneered the use of multi-echo DTI in the mid-1990s. In a series of experiments, multi-echo DTI was used to separate diffusion based on T_2 in simulations, vegetables, and healthy and occluded neural tissues (56,57). Stanisz et al. carried out similar experiments in optic nerve (58), and Does et al. in brain and facial nerves (59). The first studies using this technique in skeletal muscle were carried out by Ababneh et al. in chemically induced edematous rat paw muscles (10), and Fan et al. in a chemically induced edematous tibialis anterior (12). Although this technique is not new, these studies have demonstrated the ability to measure separate diffusion tensors, separated by the multi-T_2 decay in biological tissues. The goal of this study was to

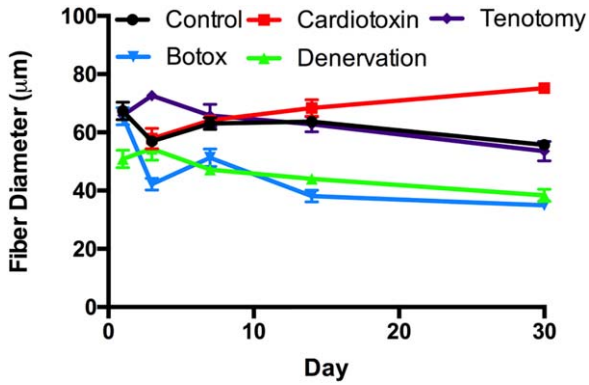

FIG. 5. Fiber diameter measurements as a function of time for control (black circles), cardiotoxin (red squares), tenotomy (purple diamonds), botox (blue upside-down triangles), and denervation (green triangles) models of skeletal muscle. Histology was obtained on Days 1, 3, 7, 14, and 30 after injury from a previous study in our lab.

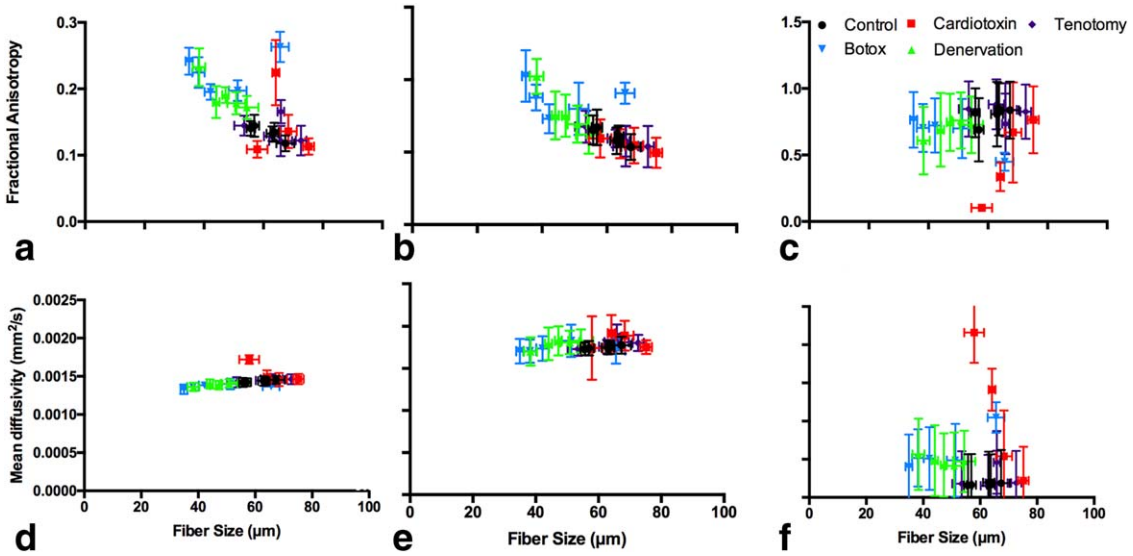

FIG. 6. Fractional anisotropy (**a**–**c**) and mean diffusivity (**d**–**f**) measurements of models with histology-informed geometry from control (black circles), cardiotoxin (red squares), tenotomy (purple diamonds), botox (blue upside down triangles), and denervation (green triangles) skeletal muscle as a function of average muscle fiber diameter. Diffusion measures were made with single-echo (**a, d**), and the short (**b, e**) and long (**c, f**) T_2 compartments from the multi-echo DTI sequence.

relate diffusion tensors calculated from multi-echo DTI to microstructural features of skeletal muscle.

In this study, we report our initial developments of a program to systematically assess these complex relationships through the use of well-defined (albeit simplistic) computational models within a DTI simulation environment. We evaluated the relationship among four microstructural features of skeletal muscle (fiber size, fibrosis, edema, and permeability) individually, and in combination with one another, and the DT in models with both simplified and histology-informed geometry. These relationships were simulated using a standard DTI and a multi-echo DTI pulse sequence, which was able to separate intra- and extracellular diffusion based on T_2 relaxation of particles in the two compartments. The main finding of this study was that fiber size is overall the strongest predictor of λ2, λ3, MD, and FA in skeletal muscle, accounting for approximately 40% of the variance in the diffusion model when calculated with single-echo DTI. This increased to approximately 70% when diffusion measures were calculated from the short T_2 compartment from multi-echo DTI, which effectively separates intra- and extracellular diffusion. Additionally, the sensitivity of diffusion measurements begins to

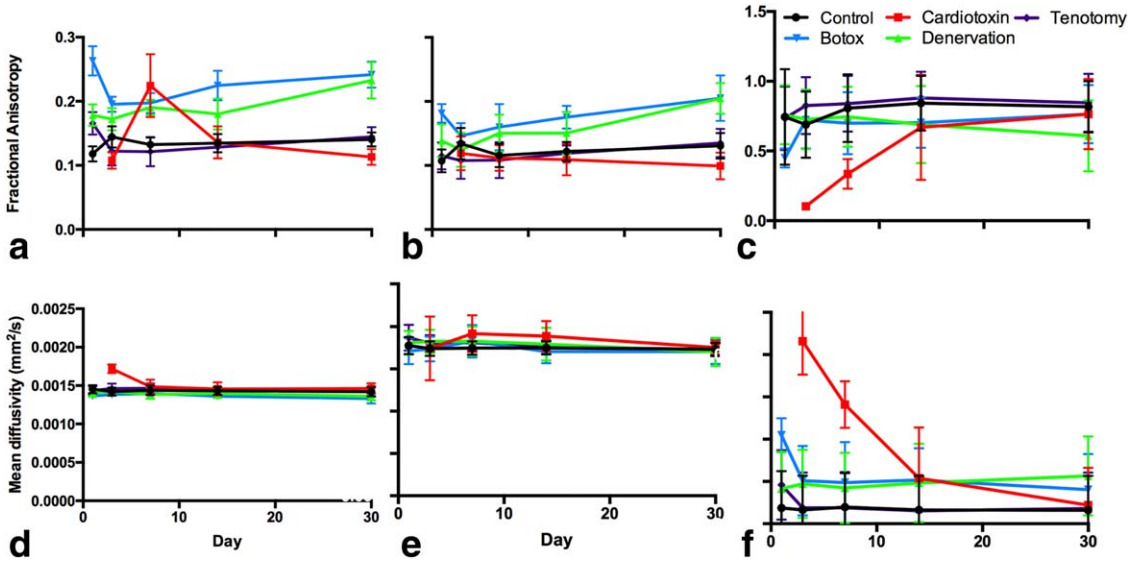

FIG. 7. Fractional anisotropy (**a**–**c**) and mean diffusivity (**d**–**f**) measurements of models with histology-informed geometry from control (black circles), cardiotoxin (red squares), tenotomy (purple diamonds), botox (blue upside-down triangles), and denervation (green triangles) skeletal muscle as a function of days after injury. Diffusion measures were made with single-echo (**a, d**), and the short (**b, e**) and long (**c, f**) T_2 compartments from the multi-echo DTI sequence.

plateau at fiber sizes greater than 60 μm. As the normal fiber size of a human muscle fiber is 40 to 60 μm (FA = 0.180–0.135), this suggests that DTI is a sensitive tool to monitor muscle atrophy, but may be limited in measurements of muscle hypertrophy. Comparing diffusion measurements made in models with simplified geometry versus histology informed geometry, we found that fiber size was able to explain 68% of the variance in FA calculated with the short T_2 compartment of the multi-echo DTI sequence. This supports the idea that multi-echo DTI may be a useful tool to monitor fiber size changes in the presence of edema.

Healthy skeletal muscle fibers are tightly packed, polygonal structures, surrounded by hierarchical layers of thin ECM. In the simplified models in this study, muscle fibers were approximated as tessellated hexagons, as they can be tightly packed and have a uniform linear spacing. Fibrosis is commonly studied using histology, and is defined as an accumulation of ECM in both the intra- and perifasicular spaces around muscle fibers, which ultimately interferes with function (2). Extracellular matrix is a dynamic structure consisting of a scaffold of connective tissue (e.g., collagen), fluid, and a variety of cells. Functionally in muscle, fibrosis results in increased whole-muscle passive stiffness. However, passive mechanical properties are not correlated with the biochemical makeup or area fraction of the ECM, even though they normally change in the same direction (2,60). Fibrosis is a complicated process that resists a precise characterization. For the purposes of the present study, fibrosis was defined as increased spacing of fibers. The restricted diffusion coefficient of water in the ECM was chosen to remain constant, as the relative volume fraction of fluid, ECM proteins, cells, and cellular debris in the extracellular space are unknown in healthy or fibrotic muscle. Edema in skeletal muscle is a complex, time-dependent process, which includes increased fluid transport across capillary beds, allowing for recruitment and migration of inflammatory cells into the damaged region to break down cellular debris (61). From a DTI perspective, the increased volume fraction of water has the largest effect on not only the overall diffusion signal, but also the overall T_2 relaxation of skeletal muscle. Therefore, edema was simplified as an increase in the overall extracellular volume fraction of water particles. The concept of permeability in skeletal muscle is often not well defined and commonly used to describe two physiologic processes or states: (i) the flux of water molecules and ions across a cell membrane; or (ii) damage to the cell membrane, which allows for flux of water molecules between the intra- and extracellular spaces. The first definition is important with respect to, for example, excitation-contraction coupling and muscle metabolism, but the second definition is related to a muscle's response to injury and may be related to impaired force production; membrane disruption tends to yield a regenerative response in muscle cells. As this second definition is more related to the microstructural changes that occur after injury in skeletal muscle, permeability was simplified in our model as fibers with walls that are randomly deleted.

In vivo, the presence of increased extracellular water caused by edema in injured muscle has been shown to strongly affect the diffusion signal, and may dominate other microstructural changes (e.g., fiber atrophy), making detection of microstructure-driven diffusion signal changes difficult to resolve. This confound can be addressed with the use of multi-echo DTI, which can distinguish between intra- and extracellular diffusion in muscle by exploiting differences in the T_2 rate of intra- and extracellular water (10,12). However, this application of multi-echo DTI, while promising, has not been well studied in muscle in vivo. To date, single-echo DTI pulse sequences have been the predominant method in muscle DTI studies, and have yielded nonspecific signal changes, making microstructural changes difficult to quantify in the presence of edema. However, multi-echo DTI has two major drawbacks. First, the duration of the scan is long (30 min to 1 h), as multiple diffusion directions must be sampled at multiple TEs. Second, multi-T_2 fitting is a nontrivial technique that is prone to errors, especially when the compartments of the T_2 decay are close. However, techniques such as nonnegative least-squares estimation and linear programming can be used to reduce the number of T_2 compartments into the smallest number of discrete terms, to provide an accurate estimation of the data. As this technique is susceptible to noise, care must be taken to maximize SNR, particularly at the shortest measured TEs.

Diffusion-weighted spin-echo echo-planar imaging is sensitive to the T_2 relaxation of tissues as a result of relatively long TEs required for diffusion weighting. One technique that can be used to maximize SNR without increasing total scan time with additional signal averages, and to adequately sample the early part of the relaxation curve, is to minimize TE. Shortening the TE in a pulse sequence is complicated by many factors, including hardware limitations, the duration of the diffusion gradients, and spatially encoding the diffusion signal with echo-planar imaging. The use of short diffusion times with short TEs in the diffusion literature is not unique to this study, but is reported across the literature in studies using a spin-echo DTI pulse sequence. Although the diffusion time used in this study was short (9 ms), short diffusion times have been used in studies using high-field strength (6.3T+) MRI with comparable TE (Δ/TE; 10 ms/25 ms in Zhang et al. (62), 10 ms/20 ms in Gineste et al. (63), 11.7 ms/29 ms in Ababneh et al. (10), 12 ms/21 ms in Fan et al. (12), 13 ms/30 ms in Heemskerk et al. (13), and 13 ms/30 ms in Heemskerk et al. (64)). In these studies, because T_2 relaxation decreases with increasing magnetic field strength, the time between diffusion gradients was shortened to minimize TE, to maximize SNR.

The main drawback of short diffusion times in spin-echo-based DTI studies is the length scale of diffusion being probed (mean square displacement of approximately 6 μm) is less than the size of a muscle fiber. This results in only a fraction of the water molecules at the start of the DTI experiment that are near the sarcolemma actually undergoing restricted diffusion, which leaves molecules in the center of the fiber undergoing "unrestricted diffusion," causing a diffusion time dependence on the

diffusion tensor. Sigmund et al. used a non-spin-echo-based DTI sequence to demonstrate that, compared with short diffusion times, long diffusion times result in a decrease in diffusivity and an increase in FA (65). This may be because with longer diffusion, a larger fraction of water molecules has the opportunity to reflect off of the main barrier to diffusion, decreasing the fraction of molecules in the center of a fiber that undergo "free diffusion." However, long diffusion times are not feasible in spin-echo-based DTI, as a result of the short T_2 of muscle. In some studies that use longer diffusion times with spin-echo-based DTI sequences, issues with SNR have been reported. For example, Hoojimans et al. (66) rejected regions of interest in muscle with SNR < 20, as inaccurate estimation of the diffusion tensor is common under this threshold as determined in (23). In an experiment using the exact pulse sequence used in this manuscript on a 7T scanner at our institution, we reported an SNR of 33.7 on a 3-dimensional (3D) printed, hydrogel diffusion phantom with muscle microstructural features (42). Similar SNR values have been measured in unreported data in skeletal muscle tissue in our lab.

One solution to balancing short transverse relaxation, TE, and diffusion duration is to use stimulated-echo DTI, which is able to sample diffusion at longer diffusion times, while minimizing the exponential signal decay resulting from transverse relaxation (8,67). Although the sensitivity of this technique to fiber size appears high in normal muscle, its sensitivity to fiber size in the presence of edema has not, to our knowledge, been studied. Moreover, stimulated-echo sequences are not standard in clinical application (most scanners do not have product stimulated-echo sequences); so, from a practical standpoint, they are less relevant to our goal of establishing clinical metrics. Therefore, we did not use a stimulated echo technique in this study, although its use will be a consideration in future studies.

Fiber size is a key metric in understanding the isometric force–generating potential of muscle (68). In this study, we found that fiber size explains approximately 70% of the variance in FA when calculated with the short T_2 compartment from multi-echo DTI. As FA decreased, fiber size increased and the theoretical force-generating capacity of muscle fibers increased. Although this finding is not in itself novel, the exponential relationship between fiber size and FA has not been previously shown. Additionally, with the diffusion sequence tested, a plateau was found for diffusion measurements in muscle fibers greater than 60-μm diameter, which is on the upper boundary of normal human skeletal muscle. Clinically, this suggests that DTI is most sensitive to monitoring atrophic disease processes in skeletal muscle.

There are several limitations to this study. First, we did not investigate the effect of SNR on the DT. Future studies of these models will add Gaussian noise to each echo of the diffusion signal to generate SNR ranging from 5 to 140, to compare with previously reported studies. Second, the estimates of extracellular water-volume fraction for histology-informed geometry models were approximated from previous MR studies of these tissues and were not histologically measured. Third, a relatively small duration of diffusion was measured, which does not allow for all of the water molecules in a cell to be restricted by the sarcolemma. Future studies should include investigating these same models with either different diffusion parameters (i.e., longer diffusion duration) or different DTI pulse sequences (i.e., stimulated-echo DTI, high angular resolution diffusion imaging, or multi-shell DTI), to get better diffusion contrast. The models in these studies were extrapolated into 3D from 2-dimensional outlines, as muscle fiber geometry is relatively uniform longitudinally in normal skeletal muscle over the diffusion distances that can be probed in a DTI experiment. Therefore, only subtle changes were observed in $\lambda 1$ (along the main axis of diffusion). Techniques such as 3D high-resolution confocal laser scanning microscopy have been used to generate 3D models for diffusion simulation in an asparagus model of diffusion (69). In future iterations of these studies, similar techniques could be used to inform models with real muscle geometry in 3D. Finally, myofilaments inside, and extracellular matrix proteins outside, of muscle fibers were not included in this model. However these elements of muscle microstructure do have an effect on intra- and extracellular diffusion (70,71). The effect of these elements on the diffusion tensor was partially accounted for by assigning diffusion coefficients measured in multiple physical studies of small macromolecules in these tissues to the intra- and extracellular compartments, respectively. In addition, DifSim partially takes into account uncertainty associated with assigning experiment-based diffusion values when determining the step length of a molecule. At the beginning of an experiment, MCell generates two look-up tables: (i) a table containing 1024 values of equally probable step lengths based on the molecules assigned diffusivity, and (ii) a table with more than 130,000 equally probable symmetric directions (41). For each step for each molecule, a step length and radial direction are chosen at random from these tables. This provides a distribution of step lengths and directions across molecules, which differs from lattice-free walk algorithms, which combine a fixed diffusion step length with random directions.

Using in silico modeling to tightly regulate microstructure provides the experimental control required to uncouple microstructure from diffusion measurements, which is impossible to perform in vivo. This was an initial study, which studied the relationship between microstructure and the DT in highly simplified, and geometrically relevant, models of skeletal muscle. This study provides the framework for future studies investigating the dependence of the relationship between the diffusion and muscle microstructure on SNR, diffusion pulse-sequence parameters, and diffusion-pulse sequences. However, the findings from this study do not provide a direct platform to translate to other acquisitions with different imaging parameters. A key interpretation of these experiments is a theoretical framework that can be used to identify features of muscle microstructure that DTI may be most sensitive to, and which combinations are beyond the sensitivity of the technique. This tool can be used by clinicians and researchers to interpret DTI data, and to noninvasively quantify muscle microstructure to aid in diagnosis, monitor disease progression, and evaluate treatment of muscle pathologies for a wide range of patients.

ACKNOWLEDGMENTS

The authors would like to thank Keaton Blazer for his help in generating the histology-informed computer models.

REFERENCES

1. Lieber RL. Skeletal muscle structure, function, and plasticity. Philadelphia, PA, USA: Lippincott Williams & Wilkins; 2002.
2. Lieber RL, Ward SR. Cellular mechanisms of tissue fibrosis. 4: Structural and functional consequences of skeletal muscle fibrosis. Am J Physiol Cell Physiol 2013;305:C241–C252.
3. Minamoto VB, Suzuki KP, Bremner SN, Lieber RL, Ward SR. Dramatic changes in muscle contractile and structural properties after 2 botulinum toxin injections. Muscle Nerve 2015;52:649–657.
4. Esposito A, Campana L, Palmisano A, De Cobelli F, Canu T, Santarella F, Colantoni C, Monno A, Vezzoli M, Pezzetti G. Magnetic resonance imaging at 7T reveals common events in age-related sarcopenia and in the homeostatic response to muscle sterile injury. PloS One 2013;8:e59308.
5. Herbison G, Jaweed M, Ditunno J. Muscle fiber atrophy after cast immobilization in the rat. Arch Phys Med Rehab 1978;59:301–305.
6. Silldorff MD, Choo AD, Choi AJ, Lin E, Carr JA, Lieber RL, Lane JG, Ward SR. Effect of supraspinatus tendon injury on supraspinatus and infraspinatus muscle passive tension and associated biochemistry. J Bone Joint Surg Am 2014;96:e175.
7. Hamer P, McGeachie J, Davies M, Grounds M. Evans Blue Dye as an in vivo marker of myofibre damage: optimising parameters for detecting initial myofibre membrane permeability. J Anat 2002;200:69–79.
8. Sigmund EE, Novikov DS, Sui D, Ukpebor O, Baete S, Babb JS, Liu K, Feiweier T, Kwon J, McGorty K. Time-dependent diffusion in skeletal muscle with the random permeable barrier model (RPBM): application to normal controls and chronic exertional compartment syndrome patients. NMR Biomed 2014;27:519–528.
9. Straub V, Rafael JA, Chamberlain JS, Campbell KP. Animal models for muscular dystrophy show different patterns of sarcolemmal disruption. J Cell Biol 1997;139:375–385.
10. Ababneh Z, Beloeil H, Berde CB, Gambarota G, Maier SE, Mulkern RV. Biexponential parameterization of diffusion and T2 relaxation decay curves in a rat muscle edema model: decay curve components and water compartments. Magn Reson Med 2005;54:524–531.
11. Bryant ND, Li K, Does MD, Barnes S, Gochberg DF, Yankeelov TE, Park JH, Damon BM. Multi-parametric MRI characterization of inflammation in murine skeletal muscle. NMR Biomed 2014;27:716–725.
12. Fan RH, Does MD. Compartmental relaxation and diffusion tensor imaging measurements in vivo in λ-carrageenan-induced edema in rat skeletal muscle. NMR Biomed 2008;21:566–573.
13. Heemskerk AM, Drost MR, van Bochove GS, van Oosterhout MF, Nicolay K, Strijkers GJ. DTI-based assessment of ischemia-reperfusion in mouse skeletal muscle. Magn Reson Med 2006;56:272–281.
14. Van Donkelaar C, Kretzers L, Bovendeerd P, Lataster L, Nicolay K, Janssen J, Drost M. Diffusion tensor imaging in biomechanical studies of skeletal muscle function. J Anat 1999;194:79–88.
15. Van Doom A, Bovendeerd P, Nicolay K, Drost M, Janssen J. Determination of muscle fibre orientation using diffusion-weighted MRI. Eur J Morphol 1996;34:5–10.
16. Deux J, Malzy P, Paragios N, Bassez G, Luciani A, Zerbib P, Roudot-Thoraval F, Vignaud A, Kobeiter H, Rahmouni A. Assessment of calf muscle contraction by diffusion tensor imaging. Eur Radiol 2008;18:2303–2310.
17. Hatakenaka M, Yabuuchi H, Sunami S, Kamitani T, Takayama Y, Nishikawa K, Honda H. Joint position affects muscle proton diffusion: evaluation with a 3-T MR system. Am J Roentgenol 2010;194:W208–W211.
18. Schwenzer NF, Steidle G, Martirosian P, Schraml C, Springer F, Claussen CD, Schick F. Diffusion tensor imaging of the human calf muscle: distinct changes in fractional anisotropy and mean diffusion due to passive muscle shortening and stretching. NMR Biomed 2009;22:1047–1053.
19. Sinha S, Sinha U, Edgerton VR. In vivo diffusion tensor imaging of the human calf muscle. J Magn Reson Imaging 2006;24:182–190.
20. Sinha U, Sinha S, Hodgson JA, Edgerton RV. Human soleus muscle architecture at different ankle joint angles from magnetic resonance diffusion tensor imaging. J Appl Physiol 2011;110:807–819.
21. Hall MG, Clark CA. Diffusion in hierarchical systems: a simulation study in models of healthy and diseased muscle tissue. Magn Reson Med 2017;78:1187–1198.
22. Sciorati C, Esposito A, Campana L, Canu T, Monno A, Palmisano A, De Cobelli F, Del Maschio A, Ascheman DP, Manfredi AA. 7-Tesla magnetic resonance imaging precisely and noninvasively reflects inflammation and remodeling of the skeletal muscle in a mouse model of antisynthetase syndrome. Biomed Res Int 2014;2014:879703.
23. Damon BM. Effects of image noise in muscle diffusion tensor (DT)-MRI assessed using numerical simulations. Magn Reson Med 2008;60:934–944.
24. Damon BM, Gregory CD, Hall KL, Stark HJ, Gulani V, Dawson MJ. Intracellular acidification and volume increases explain R2 decreases in exercising muscle. Magn Reson Med 2002;47:14–23.
25. Froeling M, Nederveen AJ, Nicolay K, Strijkers GJ. DTI of human skeletal muscle: the effects of diffusion encoding parameters, signal-to-noise ratio and T2 on tensor indices and fiber tracts. NMR Biomed 2013;26:1339–1352.
26. Belton PS, Jackson RR, Packer KJ. Pulsed NMR studies of water in striated muscle. I. Transverse nuclear spin relaxation times and freezing effects. Biochim Biophys Acta 1972;286:16–25.
27. Cole WC, Leblanc AD, Jhingran SG. The origin of biexponential T2 relaxation in muscle water. Magn Reson Med 1993;29:19–24.
28. Gambarota G, Cairns BE, Berde CB, Mulkern RV. Osmotic effects on the T2 relaxation decay of in vivo muscle. Magn Reson Med 2001;46:592–599.
29. Hazlewood CF, Chang DC, Nichols BL, Woessner DE. Nuclear magnetic resonance transverse relaxation times of water protons in skeletal muscle. Biophys J 1974;14:583–606.
30. Saab G, Thompson RT, Marsh GD. Effects of exercise on muscle transverse relaxation determined by MR imaging and in vivo relaxometry. J Appl Physiol 2000;88:226–233.
31. Nikolaou PK, Macdonald BL, Glisson RR, Seaber AV, Garrett JR WE. Biomechanical and histological evaluation of muscle after controlled strain injury. Am J Sports Med 1987;15:9–14.
32. Fung B, Puon P. Nuclear magnetic resonance transverse relaxation in muscle water. Biophys J 1981;33:27–37.
33. Farrell JA, Landman BA, Jones CK, Smith SA, Prince JL, van Zijl P, Mori S. Effects of signal-to-noise ratio on the accuracy and reproducibility of diffusion tensor imaging–derived fractional anisotropy, mean diffusivity, and principal eigenvector measurements at 1.5 T. J Magn Reson Imaging 2007;26:756–767.
34. Anderson AW. Theoretical analysis of the effects of noise on diffusion tensor imaging. Magn Reson Med 2001;46:1174–1188.
35. Pierpaoli C, Basser PJ. Toward a quantitative assessment of diffusion anisotropy. Magn Reson Med 1996;36:893–906.
36. Karampinos DC, King KF, Sutton BP, Georgiadis JG. Myofiber ellipticity as an explanation for transverse asymmetry of skeletal muscle diffusion MRI in vivo signal. Ann Biomed Eng 2009;37:2532–2546.
37. Damon B. Effect of b-value and TE on the estimation of intramyocellular diffusion properties in the presence of edema. In Proceedings of the 17th Annual Meeting of ISMRM, Honolulu, Hawaii, USA, 2009. Abstract 1435.
38. Kerr RA, Bartol TM, Kaminsky B, Dittrich M, Chang J-CJ, Baden SB, Sejnowski TJ, Stiles JR. Fast Monte Carlo simulation methods for biological reaction-diffusion systems in solution and on surfaces. SIAM J Sci Comput 2008;30:3126–3149.
39. Stiles J, Van Helden D, Bartol T, SALPETER M. Miniature endplate current rise times $<100\,\mu s$ from improved dual recordings can be modeled with passive acetylcholine diffusion from a synaptic vesicle. Proc Natl Acad Sci U S A 1996;93:5747–5752.
40. Stiles JR, Bartol TM. Monte Carlo methods for simulating realistic synaptic microphysiology using MCell. In: Computational neuroscience: realistic modeling for experimentalists. Boca Raton, FL: CRC Press; 2001. pp 87–127.
41. Balls GT, Frank LR. A simulation environment for diffusion weighted MR experiments in complex media. Magn Reson Med 2009;62:771–778.
42. Berry DB, You S, Warner J, Frank LR, Chen S, Ward SR. A 3D tissue-printing approach for validation of diffusion tensor imaging in skeletal muscle. Tissue Eng Part A 2017;23:980–988.
43. Does MD. Multiexponential relaxation analysis. 2014. http://www.vuiis.vanderbilt.edu/~doesmd/MERA/MERA_Toolbox.html. Accessed September 9, 2015.
44. Barmpoutis A, Vemuri BC. A unified framework for estimating diffusion tensors of any order with symmetric positive-definite

constraints. In Proceedings of the 7th IEEE International Symposium on Biomedical Imaging, Rotterdam, Netherlands, 2010. pp. 1385–1388.
45. Kent BR. 3D scientific visualization with blender. San Rafael, CA, USA: Morgan & Claypool; 2015.
46. Crémillieux Y, Ding S, Dunn JF. High-resolution in vivo measurements of transverse relaxation times in rats at 7 Tesla. Magn Reson Med 1998;39:285–290.
47. Diakova G, Korb JP, Bryant RG. The magnetic field dependence of water T1 in tissues. Magn Reson Med 2012;68:272–277.
48. Gefen A, Cornelissen LH, Gawlitta D, Bader DL, Oomens CW. The free diffusion of macromolecules in tissue-engineered skeletal muscle subjected to large compression strains. J Biomech 2008;41:845–853.
49. Moll W. The diffusion coefficient of myoglobin in muscle homogenate. Pflüger's Archiv für die gesamte Physiologie des Menschen und der Tiere 1968;299:247–251.
50. Papadopoulos S, Jürgens KD, Gros G. Protein diffusion in living skeletal muscle fibers: dependence on protein size, fiber type, and contraction. Biophys J 2000;79:2084–2094.
51. Gilbert DL, Okano T, Miyata T, Kim SW. Macromolecular diffusion through collagen membranes. Int J Pharm 1988;47:79–88.
52. Ramanujan S, Pluen A, McKee TD, Brown EB, Boucher Y, Jain RK. Diffusion and convection in collagen gels: implications for transport in the tumor interstitium. Biophys J 2002;83:1650–1660.
53. d'Albis A, Couteaux R, Janmot C, Roulet A, Mira JC. Regeneration after cardiotoxin injury of innervated and denervated slow and fast muscles of mammals. Eur J Biochem 1988;174:103–110.
54. Kobayashi J, Mackinnon SE, Watanabe O, Ball DJ, Ming Gu X, Hunter DA, Kuzon WM. The effect of duration of muscle denervation on functional recovery in the rat model. Muscle Nerve 1997;20:858–866.
55. Jozsa L, Kannus P, Thoring J, Reffy A, Jarvinen M, Kvist M. The effect of tenotomy and immobilisation on intramuscular connective tissue. A morphometric and microscopic study in rat calf muscles. Bone Joint J 1990;72:293–297.
56. Van Dusschoten D, Dejager PA, Vanas H. Extracting diffusion constants from echo-time-dependent PFG NMR data using relaxation-time information. J Magn Reson Ser A 1995;116:22–28.
57. Van Dusschoten D, Moonen CT, de Jager PA, Van As H. Unraveling diffusion constants in biological tissue by combining Carr-Purcell-Meiboom-Gill imaging and pulsed field gradient NMR. Magn Reson Med 1996;36:907–913.
58. Stanisz GJ, Henkelman RM. Diffusional anisotropy of T2 components in bovine optic nerve. Magn Reson Med 1998;40:405–410.
59. Does MD, Gore JC. Compartmental study of diffusion and relaxation measured in vivo in normal and ischemic rat brain and trigeminal nerve. Magn Reson Med 2000;43:837–844.
60. Smith LR, Lee KS, Ward SR, Chambers HG, Lieber RL. Hamstring contractures in children with spastic cerebral palsy result from a stiffer extracellular matrix and increased in vivo sarcomere length. J Physiol 2011;589:2625–2639.
61. Armstrong R, Warren G, Warren J. Mechanisms of exercise-induced muscle fibre injury. Sports Med 1991;12:184–207.
62. Zhang J, Zhang G, Morrison B, Mori S, Sheikh KA. Magnetic resonance imaging of mouse skeletal muscle to measure denervation atrophy. Exper Neurol 2008;212:448–457.
63. Gineste C, Duhamel G, Le Fur Y, Vilmen C, Cozzone PJ, Nowak KJ, Bendahan D, Gondin J. Multimodal MRI and 31 P-MRS investigations of the ACTA1 (Asp286Gly) mouse model of nemaline myopathy provide evidence of impaired in vivo muscle function, altered muscle structure and disturbed energy metabolism. PloS One 2013; 8:e72294.
64. Heemskerk AM, Strijkers GJ, Drost MR, van Bochove GS, Nicolay K. Skeletal muscle degeneration and regeneration after femoral artery ligation in mice: monitoring with diffusion MR imaging 1. Radiology 2007;243:413–421.
65. Sigmund EE, Sui D, Ukpebor O, Baete S, Fieremans E, Babb JS, Mechlin M, Liu K, Kwon J, McGorty K. Stimulated echo diffusion tensor imaging and SPAIR T2-weighted imaging in chronic exertional compartment syndrome of the lower leg muscles. J Magn Reson Imaging 2013;38:1073–1082.
66. Hooijmans M, Damon B, Froeling M, Versluis M, Burakiewicz J, Verschuuren J, Niks E, Webb A, Kan H. Evaluation of skeletal muscle DTI in patients with duchenne muscular dystrophy. NMR Biomed 2015;28:1589–1597.
67. Frahm J, Merboldt K, Hänicke W, Haase A. Stimulated echo imaging. J Magn Reson (1969) 1985;64:81–93.
68. Minamoto VB, Hulst JB, Lim M, Peace WJ, Bremner SN, Ward SR, Lieber RL. Increased efficacy and decreased systemic-effects of botulinum toxin A injection after active or passive muscle manipulation. Dev Med Child Neurol 2007;49:907–914.
69. Panagiotaki E, Hall M, Zhang H, Siow B, Lythgoe M, Alexander D. High-fidelity meshes from tissue samples for diffusion MRI simulations. Med Image Comput Comput Assist Interv 2010;13:404–411.
70. Aliev MK, Tikhonov AN. Random walk analysis of restricted metabolite diffusion in skeletal myofibril systems. Mol Cell Biochem 2004; 256:257–266.
71. Shorten P, Sneyd J. A mathematical analysis of obstructed diffusion within skeletal muscle. Biophys J 2009;96:4764–4778.

SUPPORTING INFORMATION

Additional Supporting Information may be found in the online version of this article.

Fig. S1. λ1 (**a–d**), λ2 (**e–h**), and λ3 (**i–j**) measurements of simplified models of skeletal muscle. Diffusion measurements were made from single-echo DTI (red circles) and the short (black squares) and long (blue triangles) T_2 compartments from the multi-echo DTI sequence. Fiber size (**a, e, i**), fibrosis (**b, f, j**), edema (**c, g, k**), and permeability (**d, h, l**) were varied over a physiologically relevant range of parameters defined in Table 1.

Fig. S2. λ1 (**a–c**), λ2 (**d–f**), and λ3 (**g–i**) measurements of models with histology-informed geometry from control (black circles), cardiotoxin (red squares), tenotomy (purple diamonds), botox (blue upside-down triangles), and denervation (green triangles) skeletal muscle as a function of average muscle-fiber diameter. Diffusion measures were made with single-echo (**a, d, g**) and the short (**b, e, h**) and long (**c, f, i**) T_2 compartments from the multi-echo DTI sequence.

Table S1. Computational Setup for the Simulation Experiments
Note: COMET is a Linux cluster at the San Diego Supercomputing Center, where most of the simulations were performed.